Alexandria Engineering Journal (2023) 70, 315–329

HOSTED BY

Alexandria University

Alexandria Engineering Journal

www.elsevier.com/locate/aej
www.sciencedirect.com

ORIGINAL ARTICLE

Application of periodic boundaries in freight train aerodynamic performance simulations

Gaopeng Liang [a,b,c], Tanghong Liu [a,b,c,*], Yutao Xia [a,b,c], Zhengwei Chen [d,e], Xiao Dong [a,b,c], Xiaodong Chen [f]

[a] *Key Laboratory of Traffic Safety on Track of Ministry of Education, School of Traffic & Transportation Engineering, Central south University, Changsha 410075, China*
[b] *Joint International Research Laboratory of Key Technology for Rail Traffic Safety, Changsha 410075, China*
[c] *National & Local Joint Engineering Research Centre of Safety Technology for Rail Vehicle, Central South University, Changsha 410075, China*
[d] *National Rail Transit Electrification and Automation Engineering Technology Research Center (Hong Kong Branch), Hung Hom, Kowloon, Hong Kong SAR, China*
[e] *Department of Civil and Environmental Engineering, The Hong Kong Polytechnic University, Hung Hom, Kowloon, Hong Kong SAR, China*
[f] *Department of Mechanical, Aerospace and Civil Engineering, The University of Manchester, Manchester, M13 9PL, UK*

Received 26 September 2022; revised 20 February 2023; accepted 25 February 2023
Available online 7 March 2023

KEYWORDS

Freight train;
Open track;
IDDES;
Periodic boundary;
Flow field;
Aerodynamic resistance

Abstract The length of long marshalling freight train and the non-streamline shape of wagon lead to more difficulties in simulating the aerodynamic performances. To simplify the simulation process of long freight trains and conserve computational resources, periodic boundary conditions and the improved delayed detached eddy simulation based on the shear-stress transport k-ω turbulence model were employed in this study. To better analyze the aerodynamic coefficients of full-scale, nine-boxcar, and periodic-boundary simulations, the pressure and viscous drag were analyzed separately. Aerodynamic coefficients and surrounding flows of freight trains obtained from periodic-boundary, full-scale, and nine-boxcar simulation methods are compared in detail to investigate the feasibility of the periodic-boundary condition for numerical simulations of long freight trains. The dependence of the computational mesh was verified in the STAR-CCM + software. Simulation results show that the deviations of drag coefficient under the periodic-boundary and full-scale conditions is 7.6 %, and that of the nine-boxcar and full-scale conditions is 5.7 %. Based on the simulated flow fields, the variations of pressure and velocity fields around the test wagon are similar in these three simulations. Besides, the distribution of detached vortices around the test wagon are similar in simulations. Moreover, locomotive has no significant influence on aerodynamic performances of the fifth wagon in the simulation of one locomotive with nine boxcars. In this study, the computing time of full-scale condition is 58 hours, and that of periodic-boundary condition

* Corresponding author.
E-mail address: lth@csu.edu.cn (T. Liu).
Peer review under responsibility of Faculty of Engineering, Alexandria University.

https://doi.org/10.1016/j.aej.2023.02.042

is one-tenth of full-scale condition. Consequently, it can be concluded that the periodic boundary is a potential choice in aerodynamic simulations of a long freight train, better balancing the simulation accuracy and efficiency.

1. Introduction

To achieve a higher transportation efficiency of a freight train, two main ways are always adopted. One is increasing the operating speed, and the other is extending the train length, i.e, marshalling more wagons in one freight unit. However, the increased operating speed and marshalling length of a freight train cause more aerodynamic problems [1]. The acceleration will increase the interaction between the freight train and the air, especially in the non-streamline region of the head of the locomotive. Thus, a higher running speed of the freight train results in more drag generated by the non-streamline structure. A longer freight train will produce greater drag than that produced by a wagon, and the drag that stems from the locomotive is no longer dominant [2]. Besides, a longer freight train delivers much more goods, but the length of freight train is usually limited by its traction and parameters of track. Drag reduction is the main aerodynamic problem of freight trains [3], and it has always been a common concern in the freight train industry.

As the reliability of numerical algorithm elevating, numerical simulations are gradually become the indispensable method for improving the aerodynamic performances of freight train, such as drag reduction and optimization of loading pattern. Maleki, Burton [4] employed the RANS and LES methods to analyzing the influence of the train gap length and loading pattern on freight train aerodynamic performance. The results showed wake shedding frequency increased as the gap size was enlarged, besides, through placing one of containers on the empty wagon decreased the drag. Li, Burton [5] performed scale-model wind tunnel test and numerical test to analyze the contributions of the gap length and location of one container wagon to the resistance. The results showed that the gap lengths of 1.77 and 3.23 times the boxcar width had greatest potential to reduce drag, and front gap size had the dominant effect on the drag variations. Maleki, Burton [6] performed a numerical simulation to demonstrate that the gap length in a double-stacked freight train affects the aerodynamic parameters, such as the drag and side forces, under crosswinds with different yaw angles. The results showed that a short gap length upstream and low yaw of the crosswind were important to the variation rate of the drag. Östh, Krajnović [7] conducted an isolated single-stacked container wagon, and a wagon was placed within wagon ahead and behind by LES method. The results showed removing ribs from container can reduce 50–60 % drag of single freight train wagon.

Long freight trains lead to many difficulties for simulating the aerodynamic performances, compared with numerical simulations on a freight train with shorter length. Furthermore, there are many kinds of typical trains, such as container, flat, and tank wagon. The length-to-height ratios of freight trains (length-to-height ratio (L/H) = 250–500) are greater than those of high-speed passenger trains (L/H = 25–200) [4,8], and the non-streamlined shape of freight train causes more complex flow fields in simulations [7]. By this conclusion, neither full-scale wind-tunnel tests nor fully resolved numerical simulations of typical wagons with such extreme lengths are possible. In railway full-scale train aerodynamic performance simulations, parallel computing is an effective method to decrease the time spent on simulating processes [9], and the parallel computing method is employed in this study. Soper, Baker [10] performed a comparative study on the wind created by containers and the surface pressures under three loading patterns via dynamic model tests. They found that the boundary layer could become stable after four container lengths when the loading rate was greater than 50 %. In contrast, the boundary layer required five container lengths to become stable when the loading rate was lower than 50 %. The boundary layers with high or low loading rates for five container lengths were stable. Thus, the length of a freight train in a simulation need to be longer than five container lengths. Golovanevskiy, Chmovzh [2] simulated open freight trains that consisted of a locomotive, and 10, 12, and 14 wagons. They found that the locomotive and the last wagon only impacted the first and last three wagons' aerodynamic performances. By this conclusion, to analyze freight train aerodynamic performance without the effects of the locomotive and last wagon, at least one wagon needs to be arranged upstream of the test wagon, and three wagons need to be arranged downstream. Watkins, Saunders [11] performed a one-tenth wind tunnel test and found no significant changes in middle wagon's aerodynamic performances when there were at least 1.5 wagons arranged upstream and 0.5 wagons arranged downstream. The results showed that the aerodynamic performances of the wagons in the middle part of the long freight train were similar. In all the references above, although the researchers obtained many critical conclusions for long freight train simulations, these conclusions cannot help reducing the time and resources required for the modeling and simulation of long marshalling freight train.

Long marshalling freight train could be seemed like repetitive elements, except three wagons closed to locomotive and one wagon closed to final wagon [2,7]. For long marshalling freight train model, middle parts have the stable and similar flow field, and these train represents whole freight train aerodynamic performances. Periodic boundary method was designed to solving these problems that consisted of repetitive and infinite elements, and it has been successfully used in airplane and ship dynamic simulations. Sadat-Hosseini, Carrica [12] performed a successful study using a periodic-boundary method to simulate dynamic performances of a ship under periodic motion. Jbeili, Zhang [13] employed periodic boundary conditions to simulate heat transfer in heterogeneous materials. Qian, Deng [14] employed a periodic-boundary method to simulate the effect of periodic heaving motion on two-

phase flow instability in parallel channels. Moreover, discrete element dates of computational fluid dynamics at periodic outlet surfaces can map to inlet surfaces in every time step. Consequently, periodic boundary can be viewed as a new and potential method to help researchers accelerating the process of studies about long marshalling freight train aerodynamic performance, such as reducing drag of long freight train and saving resources that were unnecessary consumed. In this study, the computing time spent on full-scale and periodic-boundary condition is 58 and 5.8 hours, respectively. This method was firstly introduced by those researchers studying on freight train aerodynamic performance [7]. However, the feasibility of periodic boundary conditions has also not been mentioned for freight train simulations, and even not been verified. Moreover, the results of drag and lift coefficients under RANS method were tiny than freight train experimental test, just about one-tenth of experiment test.

Generally, the periodic boundary condition has been successfully applicated in airplane and ship dynamic simulations, but the feasibility of the periodic boundary condition for numerical simulations of long freight train has not been investigated in detail. Compared with simulations with real full-length freight train model, the effects of the periodic boundary condition on numerical simulation results of aerodynamic loads and surrounding flow patterns for a long freight train are still unclear. Thus, it is important to evaluate the feasibility of periodic boundary method in freight train aerodynamic simulations before this method is introduced in long freight train numerical simulations. In this study, numerical simulations on a long freight train are conducted based on the periodic boundary conditions, real full-scale, and nine-boxcar freight train model, respectively. The aerodynamic loads and surrounding flow patterns of the simulated freight train obtained from forementioned three different simulation methods are compared in detail to systematically investigate the feasibility of the periodic boundary condition for numerical simulations of long freight train. Finally, some proposals are provided for numerical simulations of long freight trains when using the periodical boundary conditions.

2. Methodology

2.1. Model description

Boxcars can prevent goods from the rain and sunshine, and they are more stable under crosswinds [15]. Thus, boxcars have become the most popular wagons of freight trains, and they were employed in this study. The models of boxcar and locomotive employed in this study, as shown in Fig. 1, and the parameters of two models are shown in Table 1. Ltr represents the length of the model, W represents the width of the model, H represents the height of model, λ represents the ratio of the height to the width, and Str represents the model's cross-sectional area. The models that were employed in this study were like those of real wagons, and it is important to increase the reliability of results of numerical simulation.

2.2. Numerical method

There are some computational methods used to simulate the flow fields in freight train simulations, and they differ from each other. The RANS method was the typical method used in the past, and it was good for performing simulations with a low mesh density [16]. Consequently, the RANS method allowed scholars to perform simulations with low computational resources, but it was inaccurate in treating in unsteady flows near the surface of a freight train [17]. In contrast, the large eddy simulation (LES) method has high accuracy when simulating the flow around the surface of a freight train [18]. However, the LES method involves a high cost of computational resources. Neither the RANS method nor the LES method are suitable long freight train simulations. The detached eddy simulation (DES) method is a newer model that combines the merits of the RANS and LES methods. However, if the model switches between the RANS and LES methods too quickly, the flow can separate early [19]. The IDDES method inherits the merits of the delayed detached eddy simulation (DDES) and the DES method, and it has high accuracy for surface flows like the LES method. The IDDES method can also eliminate the log-layer mismatch and grid-induced separation issues. In this study, the IDDES method was adopted with periodic-boundary and full-scale conditions.

The SST k-ω turbulence model was employed in this study. Using this model, the delayed turbulent vortices could easily be captured in the simulations. The SST k-ω model of the DES method also combines the features of the SST k-ω model of the RANS or LES methods in unsteady flow boundary layers. The momentum equations for the RANS and LES methods can be defined respectively as follows:

$$\frac{\partial(\rho\,\bar{v})}{\partial t}+\nabla\cdot\left(\rho\,\bar{v}\otimes\bar{v}\right)=-\nabla\cdot\bar{p}\,I_t+\nabla\cdot\left(T+T_t^{RANS}\right)+f_b \tag{1}$$

$$\frac{\partial(\rho\,\tilde{v})}{\partial t}+\nabla\cdot\left(\rho\,\tilde{v}\otimes\tilde{v}\right)=-\nabla\cdot\tilde{p}\,I_t+\nabla\cdot\left(T+T_t^{LES}\right)+f_b \tag{2}$$

where ρ is the density, $\bar{v}$ is the velocity of the RANS method, $\tilde{v}$ is the velocity of the LES method, $\bar{p}$ is the pressure of the RANS method, $\tilde{p}$ is the pressure of the LES method, I_t is the identity tensor, T is the stress tensor, and f_b represents the resultant of the body forces.

The Reynolds-stress tensor T_t^{RANS} and T_t^{LES} can be defined respectively as follows:

$$T_t^{RANS}=f\left(\nabla\cdot\bar{v},k,\varepsilon\right) \tag{3}$$

$$T_t^{RANS}=f\left(\nabla\cdot\tilde{v},\Delta\right) \tag{4}$$

The transport equations for the kinetic energy k and the specific dissipation rate ω can be defined as follows:

$$\frac{\partial(\rho k)}{\partial t}+\nabla\cdot\left(\rho\,\bar{V}k\right)=\nabla\cdot\left[(\mu+\sigma_k\mu_t)\nabla k\right]-P_k-\rho\beta^*f_{\beta^*}(\omega\,\breve{k}-\omega_0k_0)+S_k \tag{5}$$

$$\frac{\partial(\rho\omega)}{\partial t}+\nabla\cdot\left(\rho\,\bar{V}\omega\right)=\nabla\cdot\left[(\mu+\sigma_\omega\mu_t)\nabla\omega\right]-P_\omega-\rho\beta f_\beta(\omega^2-{\omega_0}^2)+S_\omega \tag{6}$$

$$\breve{\omega}=\frac{\sqrt{k}}{l_{HYBRID}\beta^*f_{\beta^*}} \tag{7}$$

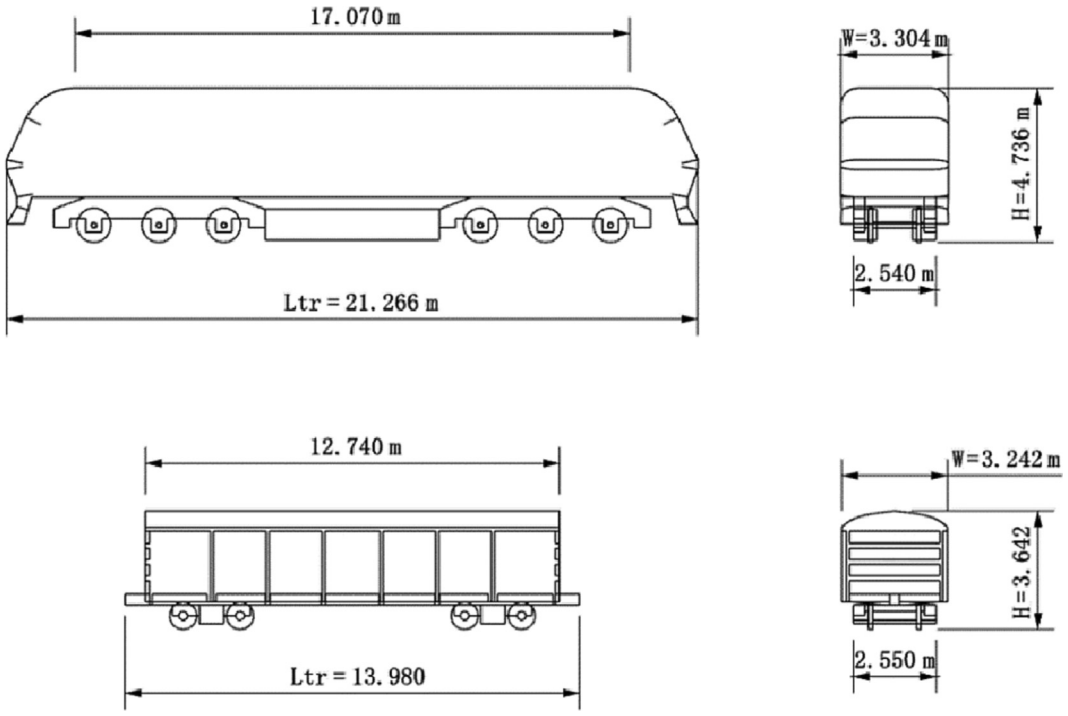

Fig. 1 Geometries of locomotive and wagon.

Table 1 Parameters of freight train models.

Model	Ltr/m	W/m	H/m	λ = H/W	Str/m^2
Locomotive	21.266	3.304	4.736	1.433	10.947
Boxcar	13.980	3.242	3.642	1.123	7.389

$$l_{HYBRID} = \tilde{f}_d(1+f_e)l_t + (1-\tilde{f}_d)C_{DES}\Delta_{IDDES} \tag{8}$$

where $\bar{V}$ is the mean velocity, μ is the dynamic viscosity, σ_k and σ_ω are model coefficients, P_k and P_ω are production terms, f_{β^*} is the free-shear modification factor, f_β is the vortex-stretching modification factor, S_k and S_ω are the specified source terms, k_0 and ω_0 are the ambient turbulence values that counteract turbulence decay [18,20].

Mach number of incoming flows (120 km/h, Ma less than 0.3) was less than 0.3 in this study. Thus, incoming flow was incompressible [21]. For differential equation of solving of an incompressible flow, incompressible finite-volume solver and the SIMPLE (semi-implicit method for pressure linked equations) pressure–velocity coupling method were employed in periodic-boundary, nine-boxcar and full-scale simulations. In finite-volume solver, the differential scheme of convection term is a matter of which adjacent points on the interface are interpolated. Therefore, differential scheme of convection term is mainly to create the interpolation scheme of $\varphi_{i+1/2}$ and $\varphi_{i-1/2}$. The relationship can be defined as:

$$u\frac{\partial\varphi}{\partial x}\bigg|_i \cong \frac{u_i}{\Delta x}(\varphi_{i+1/2} - \varphi_{i-1/2}) \tag{9}$$

SIMPLE is a representative algorithm of pressure-modified method [22,23]. The convective terms were solved by a mixed numerical scheme that contains bounded central-differencing scheme and second-order upwind scheme [22,24]. The physical time of three numerical simulations is 3.0 s, and the time step is 1.00×10^{-3} s.

For the calculation of the flow field of an incompressible fluid, the differences of the pressures between the points in the flow field are of interest, rather than their absolute values. When performing a numerical calculation using the absolute levels of stress, the calculation of the pressure difference will lead to an absolute pressure of zero. Consequently, the pressure difference of the numerical simulations were compared rather than the absolute pressure values. The drag coefficient (C_d) and lift coefficient (C_l) of the numerical simulations were also compared, and they are defined as follows:

$$C_d = \frac{F_x}{0.5\rho v^2 S} \tag{10}$$

$$C_l = \frac{F_z}{0.5\rho v^2 S} \tag{11}$$

where F_x is the resistance of the wagon, F_z is the lift force of the wagon, v is the velocity of the flow, and S is the area of the cross section of the wagon.

2.3. Computational domain and boundary conditions

Length of the full-scale simulation needs to guarantee simulated aerodynamic performances of the middle wagon of freight train accurate. According to the results of previous studies, a full-scale simulation that consists of one locomotive and nine wagons is acceptable for this study [2,9]. The nine-boxcar simulation is used to ensure that the locomotive has no significant effects on aerodynamic performance of the middle wagon of long marshalling freight train. The periodic boundary conditions consisted of two boxcars, and a 0.5 wagon was arranged upstream and downstream of the middle wagon [4]. Details of three computational domains of the full-scale, nine-boxcar, and periodic boundary simulations are shown in Fig. 2(a), 2(b), and Fig. 2(c), respectively. The incoming flows of three numerical simulations are uniform models, and the flow conditions are the same as in previous study [2]. Besides, the uniform incoming flow is effectively a simplification of more complex wind tunnel tests to simulate the movement of railway train over the ground with an atmospheric boundary layer [25], and the uniform incoming flow was widely used in aerodynamic simulations of railway train [2,19–20]. The standard distance W is the width of the boxcar, and it has shown in Table 1. Incoming flows of three numerical simulations are from left to right, and flow direction is consistent with the positive X-direction. Positive Z-direction is from bottom to top, and lift coefficient is determined along this direction.

Surfaces of inlet and outlet are periodic interfaces, and discrete dates of outlet surface map to inlet surface regularly in every time step. In this way, the test wagon in the periodic-boundary simulations could be viewed as an infinitely long freight train. Details of boundary condition of surface of three simulations are shown in Fig. 2. The no-slip condition is employed on the ground, besides, velocity component of streamwise direction is set equal to the free stream velocity [26–28].

2.4. Meshing strategy

The periodic-boundary, full-scale, and nine-boxcar simulations all used trimmed meshes and are constructed by using grid generator of the STAR-CCM + software. Grids of inlet and outlet surfaces in the periodic-boundary simulation are conformal grids, as mentioned above, discrete nodes on inlet and outlet surfaces of the periodic-boundary simulation have the same topological relationship. Besides, distance of conformal motion mapping is the length of domain of periodic-boundary simulation. Details of conformal mapping are shown in user guide of software STAR-CCM + [29].

Two different meshing parameters of full-scale simulation were arranged to prove the independence of computational grids. The first was called the coarse grid, and the second was called the fine grid. Moreover, results of aerodynamic coefficients are shown in Fig. 3(a) and (b). As Fig. 3(a) and (b) shown, differences of aerodynamic coefficients were very tiny, even it was not much than 1 %. Therefore, the coarse grid was a suitable meshing strategy in this study. To capture the flow near the bogie of the freight train, refinement region 1 was employed in the numerical simulations. To better simulate the flow field around the test wagon, refinement region 2 was

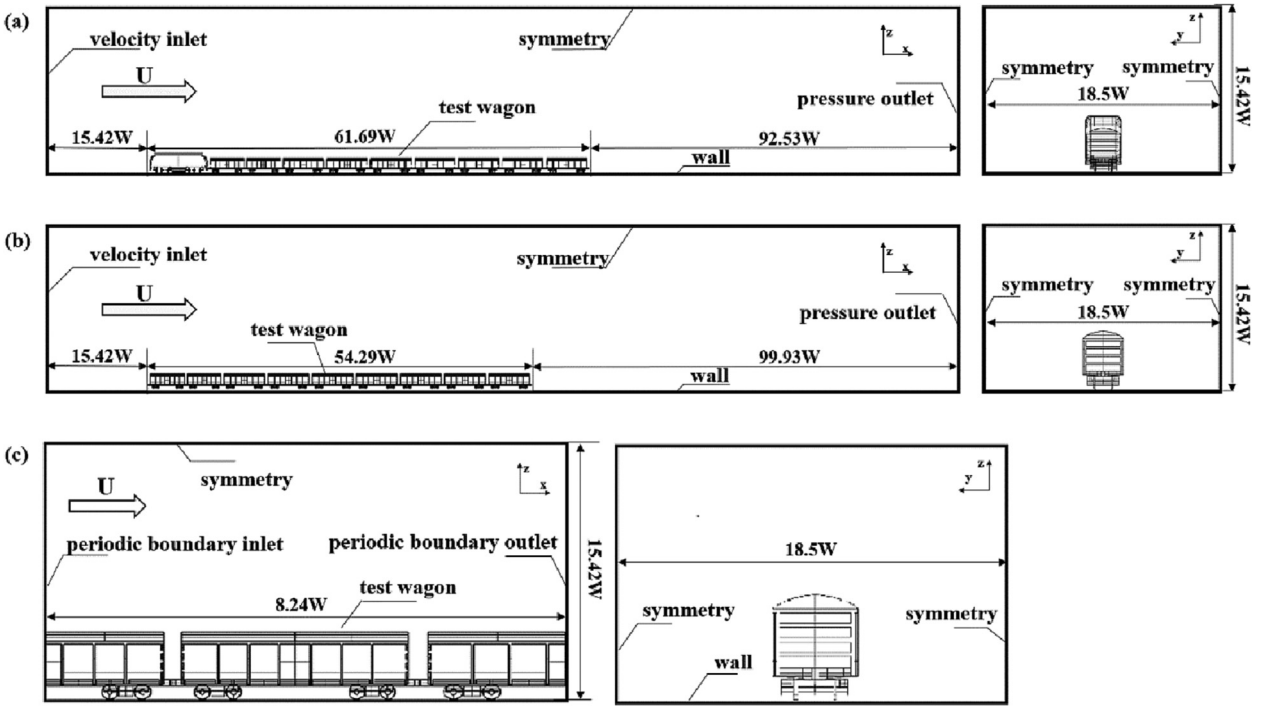

Fig. 2 Computational domain and boundary conditions: (a) full-scale conditions, (b) nine-boxcar conditions, and (c) periodic-boundary conditions.

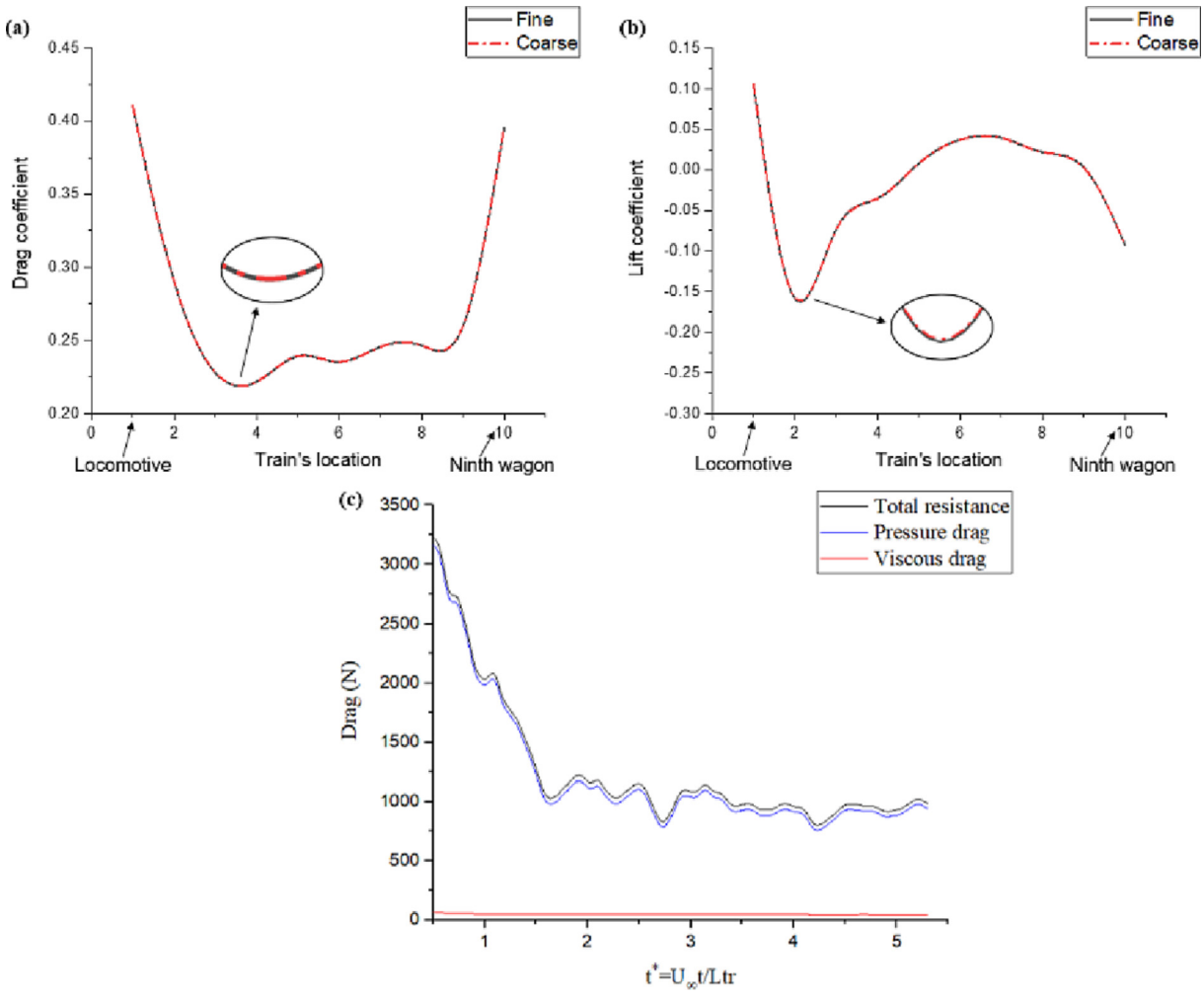

Fig. 3 Results of aerodynamic coefficients and drags: (a) drag coefficient, (b) lift coefficient, (c) pressure and viscous drag.

employed in the numerical simulations. Refinement regions of the three numerical simulations are shown in Fig. 4. In the full-scale simulation, the coarse grid contained 25 million cells, and the fine grid contained 50 million cells. In the periodic-boundary simulation, the coarse grid contained 1.3 million cells. In the nine-boxcar simulation, the coarse grid contained 24.7 million cells. The difference between coarse and fine grids is 25 million cells, two meshing types are successful in proving the independence of computational grids.

Secondly, Pressure and viscous drags of the periodic-boundary simulation are shown in Fig. 3(c). In Fig. 3(c), t* is the dimensionless time, U_∞ is the velocity of the flow, t is

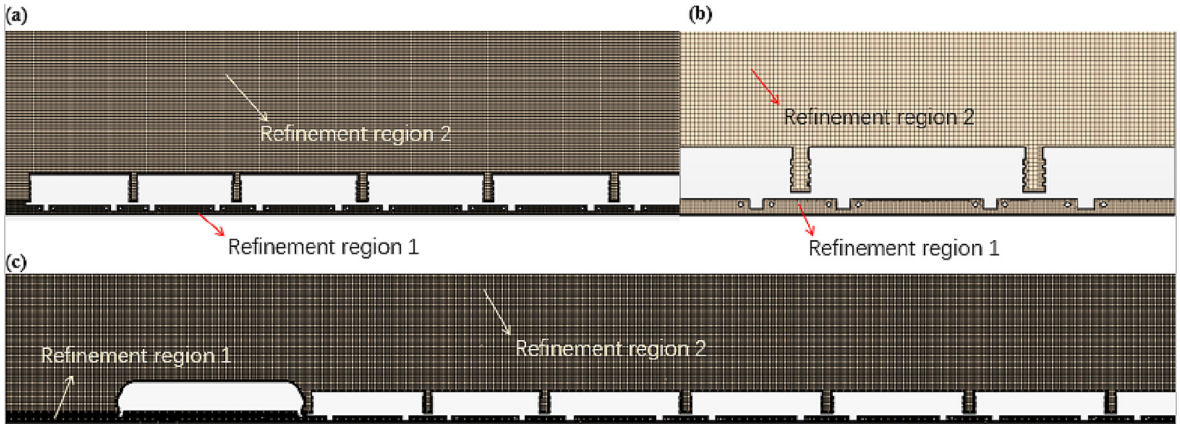

Fig. 4 Refinement of computational domain: (a) nine-boxcar simulation, (b) periodic-boundary simulation, and (c) full-scale simulation.

the physical time of the calculations, and Ltr is the length of the boxcar. From the results of resistances, some conclusions can be deduced easily. Pressure drag is the main resistance in freight train simulations, and the calculation process became nearly constant when t* reached 3.5. Therefore, pressure field is significant for the analysis of freight train aerodynamic coefficients, and aerodynamic coefficients can be derived from the time-averaged values from t* = 3.5 to 5 (ratio of resistance standard deviation with mean of resistance is 5.3 %).

3. Results and discussion

3.1. Analysis of pressure and velocity fields around test wagon

The lift and drag coefficients of three simulations are shown in Table 2, and values of lift and drag coefficients of freight train simulations are comparable to those of a previous study [2]. To show the pressure field around the test wagon more clearly, four lines around test wagon were employed in the numerical simulations. Lines A and B were employed to examine the gap flow between two wagons. Lines C and D were employed to examine the flow around the bogie and body of the test wagon. These lines are shown in Fig. 5, and Line B was located at the same location as Line A but at the rear face. The means of the pressure results of the four lines are shown in Fig. 6, and the means of the velocity magnitude results are shown in Fig. 7. The flow in the numerical simulations was from left to right. The means of the pressure and velocity magnitude results of the three numerical simulations were generally coupled.

3.1.1. Pressure and velocity fields in gap region

For Line A, because the detached vortices at the roof area and the flow did not pass though Z = 0 m on Line A, the means of the pressure and velocity magnitude at this point had low numerical values in the three simulations. As shown in Fig. 7 (a), the mean velocity magnitudes at Z = 0 m in the three numerical simulations were not significantly different. However, the means of the pressure results were significantly different, as shown by the mean pressure curves. As shown in Fig. 6 (a), the pressure value at Z = 0 m in the full-scale simulation was positive, the pressure value under the nine-boxcar simulation was lower than that in the full-scale simulation but remained positive, and in the periodic-boundary simulation, the pressure was negative. In the three numerical simulations of this study, a higher value of the velocity magnitude at the initial point led to a higher value of the pressure at the initial point. However, within a single numerical simulation, the values of the pressure were determined by the velocity differences between adjacent points. This was the reason that the pressure value at Z = 0 m on Line A in the periodic-boundary simulation was the lowest. The velocity changes of Line A in the three simulations were similar. The mean pressure curves of the three simulations were similar but appeared to be shifted, as shown in Fig. 6(a).

Along Line A from the bottom to the top direction, the mean velocity magnitude curve from Z = 0 to 0.5 m underwent one rapid variation, whereas the mean pressure curve initially dropped and then increased in this region. The pressure and velocity curves in one numerical simulation varied oppositely, as mentioned above. From Z = 0.5 to 1.8 m, the mean velocity magnitude curves in the three numerical simulations did not undergo any rapid variations. Consequently, the mean pressure curves in three numerical simulations remained around the same value from Z = 0.5 to 1.8 m. From Z = 1.8 to 2.4 m, the main detached flow distributed by impacting the front surface of the wagon was close to Line A, and then it arrived at the center of the impacted area. Because the speed of this detached flow was higher than that of the flow from Z = 0.5 to 1.8 m, the mean velocity magnitude first increased. However, along Line A in the impacted area, the mean velocity magnitude decreased sharply. This corresponded to the mean pressure curve decreasing stably at first and then rapidly increasing to the maximum. From Z = 2.4 to 2.6 m along Line A, the flow gradually left the center of impacted area and met the flow that had not impacted the front surface of the wagon. Because this flow was high-speed flow, the mean velocity magnitude increased rapidly, and the mean pressure decreased sharply. Then, the value of the mean pressure reached a minimum at Z = 2.6 m. However, the region from Z = 2.6 to 5 m along Line A was sufficiently far from the test wagon, and the value of mean pressure and velocity magnitude reached the value of the surroundings.

For Line B, because of the flow near the face of the test wagon that entered the freight train gap, a negative pressure zone was produced at the front face of the test wagon roof, and meanwhile, there was a positive pressure zone at the rear face of the previous wagon roof. The rear face of the test wagon also had a positive pressure zone, and the flow that entered the gap region also impacted the rear face after impacting the next wagon's front face. This was the reason that the mean maximum and minimum pressure value of the rear face was higher than that of the front face. This phenomenon also reflected the mean velocity magnitude curve, and the value of the mean velocity magnitude along Line B was basically always higher than that along Line A. The mean velocity magnitude at Z = 0 on Line B was also not affected by the flow, so the value of the velocity magnitude started at a low numerical value. Although the means of the velocity magnitude at Z = 0

Table 2 Aerodynamic coefficients of test wagon and computing time in simulations.

Simulations	Drag coefficient	Relative deviation	Lift coefficient	Computing time (hours)
Periodic-boundary condition	0.193	7.6 %	−0.012	5.8
Full-scale condition	0.209	5.3 %	0.006	58
Nine-boxcar condition	0.221	5.7 %	0.035	65
Wind tunnel test [2]	0.198		0.005	

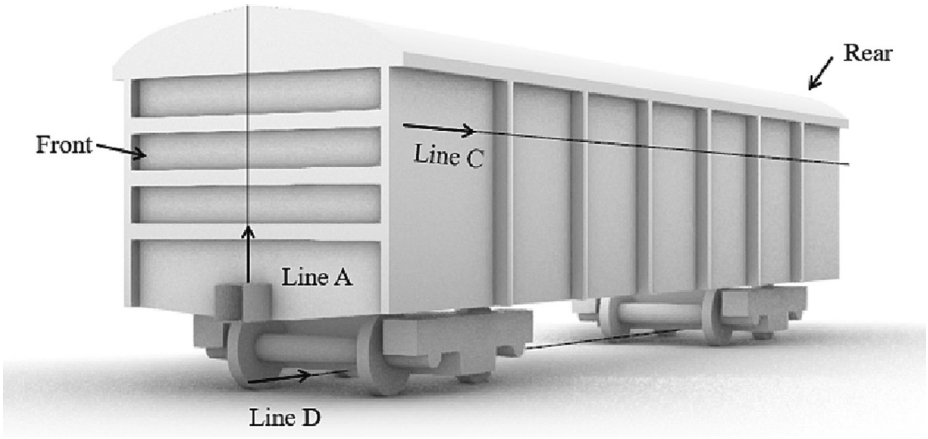

Fig. 5 Four lines employed in numerical simulations.

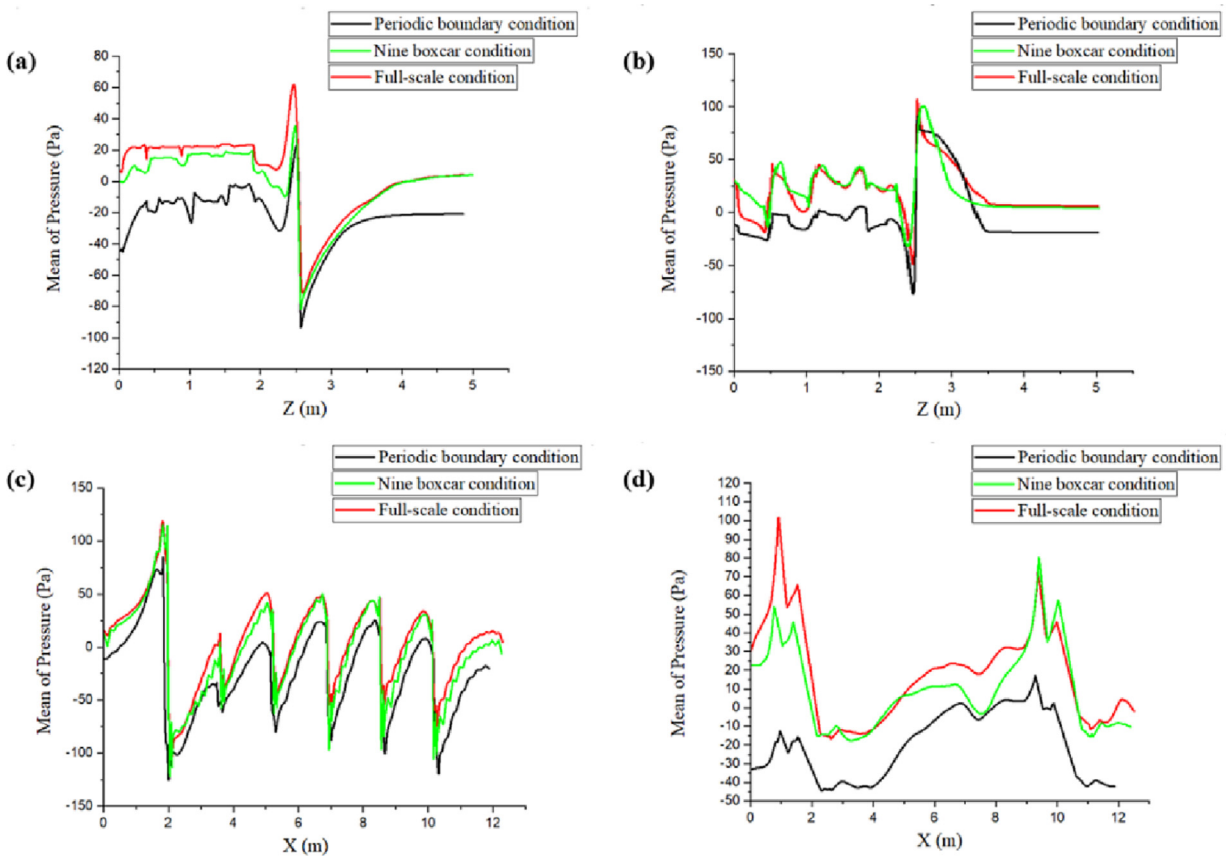

Fig. 6 Mean pressures along four lines around test wagon: (a) Line A, (b) Line B, (c) Line C, and (d) Line D.

on Lines A and B were similar, the mean pressure at Z = 0 on Line B was higher than that on Line A. The reason that the deviations of the pressure value of Lines A and B at Z = 0 were so large was as follows. As mentioned above, the pressure value was decided by the velocity values of adjacent points in a single simulation, and the velocity magnitude curve of Line B from Z = 0 to 0.5 m had two extreme points. Two extreme points meant that two rapid variations occurred, and the rapid variations on Line B were sharper than those on Line A. This was the reason that Line B had a high pressure value at Z = 0.

Along Line B from the bottom to the top direction, the mean velocity magnitude curve from Z = 0 to 0.5 m underwent two rapid variations, which was reflected by the mean pressure curve undergoing two initial drops and rises in this region. The first pressure rise in Fig. 7(b) was not most significant, but it still was evident in the mean pressure curve. Then, from Z = 0.5 to 1.5 m, the mean velocity magnitude curve of the numerical simulations still underwent four rapid variations, as did the mean pressure curve. From Z = 1.5 to 1.8 m, Line B was close to the main detached flow that was dis-

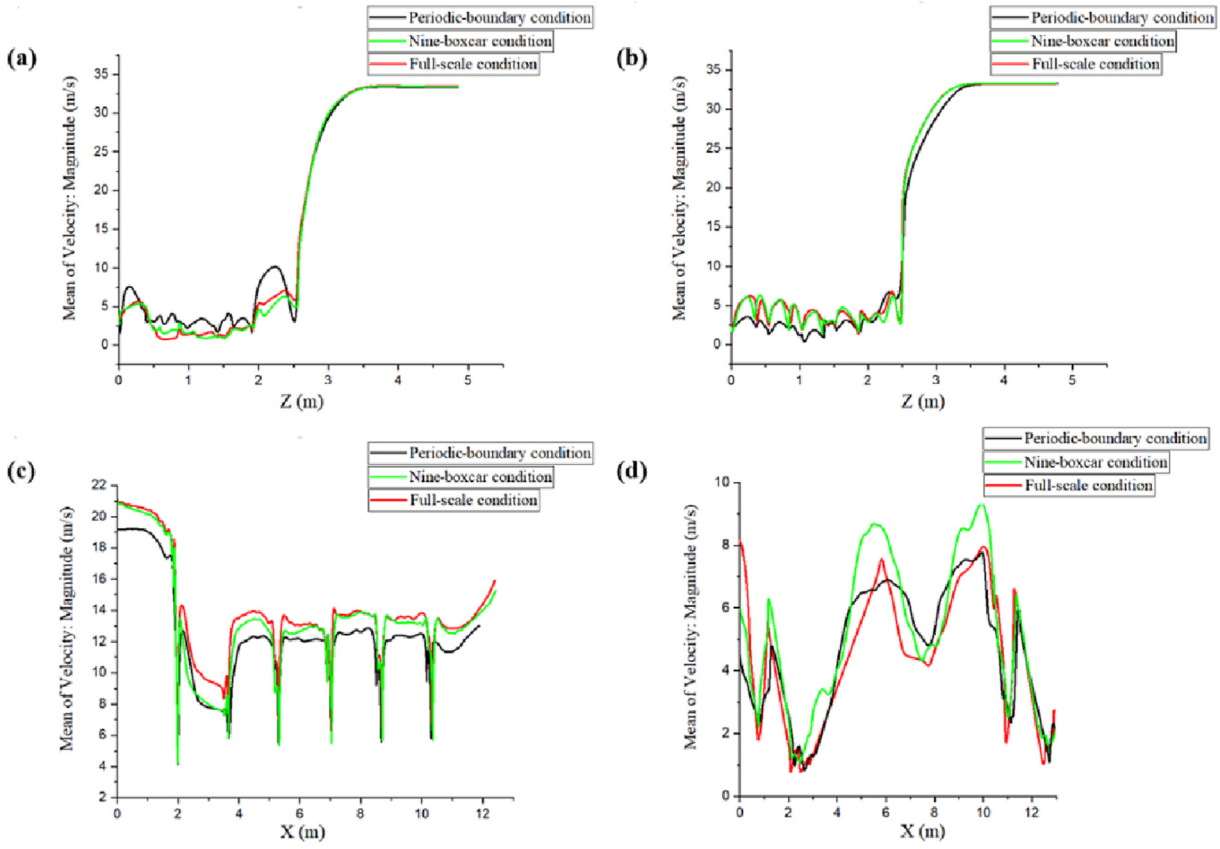

Fig. 7 Mean velocity magnitudes along four lines around test wagon: (a) Line A, (b) Line B, (c) Line C, and (d) Line D.

tributed by impacting the front surface of the next wagon, after which it arrived at the center of the area that was impacted by the flow. Because the distributed flow had a high speed, the mean velocity magnitude increased first. The velocity increase led to a pressure decrease, and consequently, the mean pressure had the minimum value. However, at the center of the impacted area of the rear face on Line B, the mean velocity magnitude decreased immediately. In the center of the impacted area, the mean velocity magnitude obtained the minimum value, and the mean pressure obtained the maximum value. From Z = 1.8 to 2.4 m along Line B, the flow gradually left the center of impacted area and met the flow that entered the freight train gap. The detached flow in the freight train gap stemmed from the flow that entered the gap region, which was high speed flow. Thus, the mean velocity magnitude increased correspondingly. From Z = 2.4 to 2.5 m, Line B left this flow and met the outside flow near the roof of the test wagon. This was reflected by the mean velocity magnitude decreasing from Z = 2.4 to 2.5 m. From Z = 2.5 to 5 m, Line B was far from test wagon, and the values of the mean pressure and velocity magnitude reached the value of surroundings.

3.1.2. Pressure and velocity field near side surface

Along Line C, the flow near the face of the test wagon that impacted the plate of the test wagon produced a positive pressure zone and a negative pressure zone on the plate upstream and downstream, respectively. There were six plates of the boxcar model, which was reflected by the mean pressure curve undergoing six rapid variations. This phenomenon was also reflected in the mean velocity magnitude curve. In Fig. 7(c), the mean velocity magnitude at X = 0 under the full-scale condition was the largest, followed by that under the nine-boxcar condition, and that under the periodic-boundary condition was the minimum. Thus, in Fig. 6(c), the mean pressure at X = 0 under the full-scale condition was largest, followed by that under the nine-boxcar condition, and that under the periodic-boundary condition was the minimum.

Along the Line C from left to right, the mean velocity magnitude curve from X = 0 to 2.0 m underwent one rapid variation, and it was reflected by the mean pressure curve initially rising and falling from X = 0 to 2.0 m. There was another small velocity decrease upstream of the first plate, and it was fully caused by viscous resistance of the flow along the test wagon side surface. Under the influence of viscous resistance, the mean velocity magnitude decreased from 21 to 18 m/s before impacting the first plate, and then the flow impacted the first plate directly. As shown in Fig. 6(c) and 7(c), this flow produced maximum and minimum values of the mean pressure along Line C and created a large negative pressure zone that affected the flow field of the second plate. When flow entered the X = 2.0 to 4.0 m region, the mean velocity magnitude curve underwent one rapid variation, and it was reflected by the mean pressure curve stably rising first and then sharply dropping. The negative pressure zone generated by first plate caused the mean pressure on the second plate upstream to be a negative value, and it was the only negative value that appeared upstream of the plates of Line C. When the flow moved from X = 4.0 to 12.0 m, the mean velocity magnitude

curve of the third plate to the sixth plate followed similar variations. The mean pressure curve varied opposite to the velocity magnitude curve, and the initial numerical deviations for three simulations remained.

3.1.3. Pressure and velocity field of bogie region

Along Line D, because the bottom flow of the freight train impacted the bogie of the test wagon, it produced a positive pressure zone and negative pressure zone of the bogie upstream and downstream, respectively. There were two bogies on the test wagon, so the bottom flow produced two main pressure zones in the freight train simulations. As shown in Fig. 7(d), the mean velocity magnitude at X = 0 under the full-scale condition was the largest, followed by that under the nine-boxcar condition, and that of the periodic-boundary condition was the minimum. Thus, as shown in Fig. 6(d), the mean pressure at X = 0 under the full-scale condition was the largest, followed by that under the nine-boxcar condition, and that under the periodic-boundary condition was the minimum.

Along the bottom, flow entered the region of the first bogie, and the mean pressure curve underwent two rapid variations in first bogie region. The first rapid variation occurred when bottom flow impacted the first wheel set of the first bogie, and the second occurred when the bottom flow impacted the framework of the first bogie. Because the cross section of the framework of the bogie was larger than the wheel set, the framework blocked much of the flow for the second wheel set of bogies. This was the reason that the main pressure zone generated by the bottom flow only had two extreme points. When the bottom flow entered the gap region between the two bogies, the gap region for the flow was an accelerating region, as shown in Fig. 8(d). Not all flows impacted the bogie, and some flows bypassed the bogie via track. The flow that bypasses the bogie also entered the accelerating region, and it helped the low-speed flow recover its original velocity. Particularly in nine-boxcar condition, the accelerating effects of the bypassing flow were the best, which helped the bottom flow to create the maximum mean pressure value in the second bogie region. Under most circumstances, the velocity increasing will lead to the pressure decreasing. However, under the nine-boxcar condition, the convex plates of the body surface led to the pressure increasing, and a large cross section of the first bogie led to a low velocity value of the starting point of the accelerating region. This was the reason for the increase in the pressure and velocity magnitude from X = 4 to 6 m. The convex plates of the boxcar created two small positive pressure zones at X = 6 and 8 m. Thus, the convex plates generated one negative pressure zone at the middle point between X = 6 and 8 m. As a result, the mean pressure and velocity magnitude curves were both decreasing from X = 6 to 7 m. When flow entered the region of the second bogie, the mean pressure curve underwent two rapid variations in the second bogie region, which was reflected by mean the velocity magnitude curve undergoing two converse rapid variations. Under the effects of the accelerating region, the nine-boxcar and periodic-boundary cases achieved their maximum velocity magnitudes in the second bogie region, which was reflected by the maxima of their mean pressure curves appearing in the second bogie region. The maximum pressure value of the nine-boxcar condition was higher than that of the full-scale condition. The maximum pressure under the full-scale condition was generated in the first bogie region, as shown in Fig. 6(d). The two extreme points of the second bogie region appeared in the first wheel set and framework, similar to those of the first bogie.

Based on the analysis of the mean pressures and velocity magnitudes on the four lines, the mean pressure curves for the three numerical simulations varied similarly. Although the mean velocity magnitude curves in three numerical simulations had differences, they were basically similar to each other.

3.2. Analysis of flow structure around test wagon

3.2.1. Flow structure of $y = 0$ plane

Three planes containing four lines were used in the three simulations, as shown in Fig. 8. The flow streamlines along the $y = 0$ plane for the periodic-boundary, full-scale, and nine-boxcar conditions are shown in Fig. 9(a), 9(b), and 9(c), respectively. In Fig. 9, the flow was from left to right. The bottom flow streamlines in the $y = 0$ plane of the full-scale condition were compared with those under the nine-boxcar condition, and the nine-boxcar condition had a higher mean velocity magnitude for most of the bottom flow. The mean velocity magnitude curve of Line D proved this, as shown in Fig. 7(d). The locomotive affected the value of the mean pres-

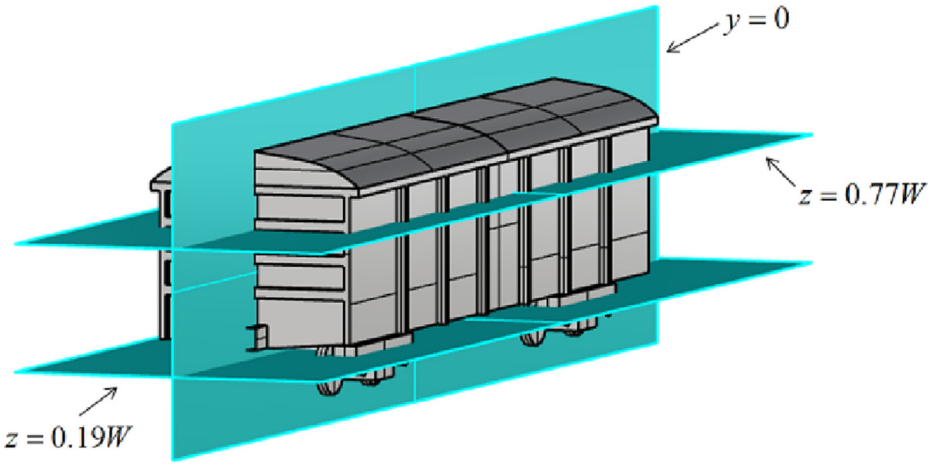

Fig. 8 Planes used to plot streamlines and flow fields around the test wagon.

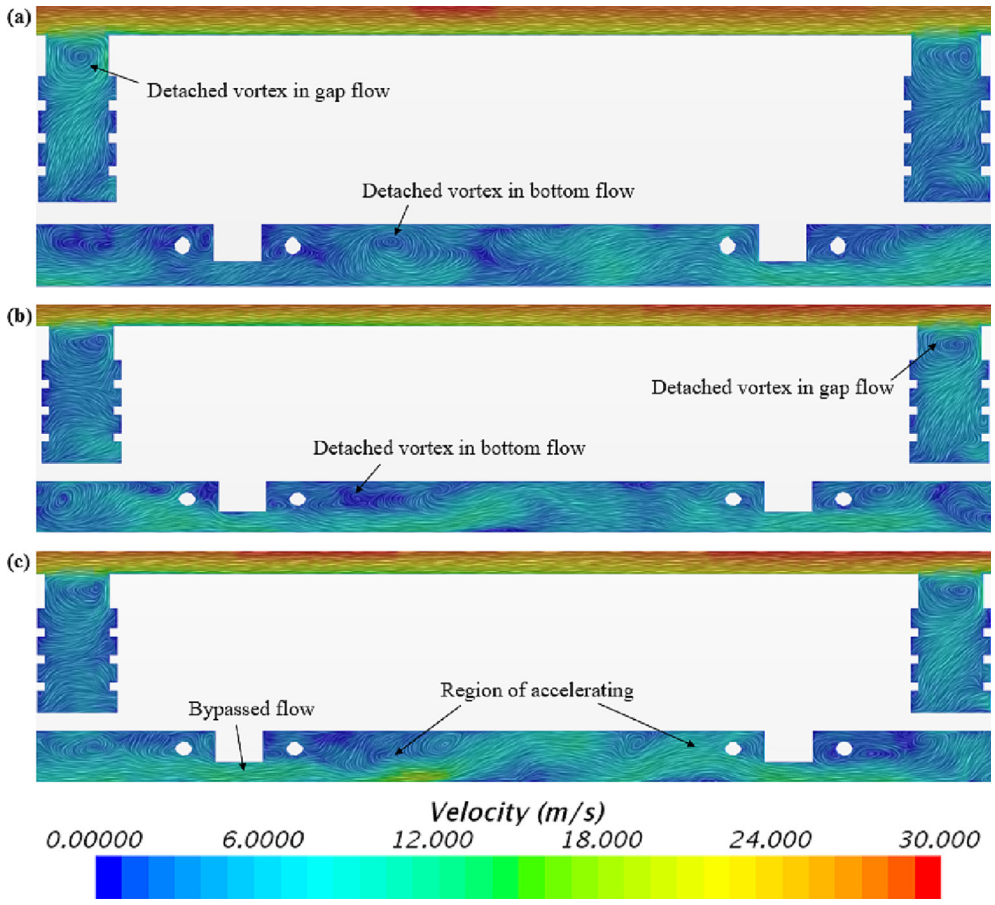

Fig. 9 Flow streamlines in $y = 0$ plane: (a) periodic-boundary condition, (b) full-scale condition, and (c) nine-boxcar condition.

sure and velocity magnitude at some points, but it did not influence the mean pressure variations of the test wagon. Due to the influence of the locomotive, the mean pressure and velocity magnitude of Line D at the initial point under the full-scale condition were higher than those under the nine-boxcar condition. Otherwise, the values at the initial point of Line D were lower than those under the nine-boxcar condition. A higher velocity magnitude in the bottom flow corresponded to fewer detached vortices in the bottom flow. Detached vortices can lead to a reduction of the ambient pressure, and a larger reduced pressure zone can lead to a lower lift coefficient (Z-axis is the positive direction). Thus, it is reasonable that the nine-boxcar condition yielded a higher lift coefficient than the full-scale condition. The gap flow streamline in the $y = 0$ plane of the full-scale condition was compared with that of the nine-boxcar condition, and the detached vortex structure in the gap region had no significant differences in the two numerical simulations. Consequently, it was deduced that the drag coefficients under the full-scale and nine-boxcar conditions were similar.

The flow streamlines in the $y = 0$ plane of periodic-boundary and full-scale conditions were compared. There were no significant differences in the vortex structures of the gap flows in the upstream and downstream regions, but detached vortices of the bottom flow under the periodic-boundary condition were stronger than those under the full-scale condition. A strong vortex resulted in a high velocity difference of the vortex. Fig. 9(a) shows that there were more low-speed vortices in the bottom flow. In Fig. 7(d), the mean velocity magnitudes under the periodic-boundary condition in the first and second bogie regions were lower than those under the full-scale condition. This was the reason that the detached vortices of the bottom flow under the periodic-boundary condition were stronger than those under the full-scale condition. Detached vortices created a greater pressure reduction, and the lift coefficient under the periodic-boundary condition turned from positive to negative. The comparison of Fig. 9(a), 9(b), and 9(c) showed that the gap flows along the $y = 0$ plane in the three numerical simulations were nearly the same. Thus, their drag coefficients were also nearly the same. This conclusion can be proven by the means of the pressure curves of Lines A and B. As shown in Table 2, the periodic-boundary condition yielded the lowest drag coefficient, followed by the full-scale condition, and finally, the nine-boxcar condition. The lift coefficients had the same order of magnitude as the drag coefficients.

3.2.2. Flow structure of $z = 0.77\ W$ plane

Flow streamlines in the $z = 0.77\ W$ plane under the periodic-boundary, full-scale, and nine-boxcar conditions are shown in Fig. 10(a), 10(b), and 10(c), respectively. As shown by the flow streamlines in the $z = 0.77\ W$ plane for the full-scale and nine-boxcar conditions, there were no significant differences in the vortex structures in the upstream and downstream flow regions, and the vortex structures of the side flow in the two

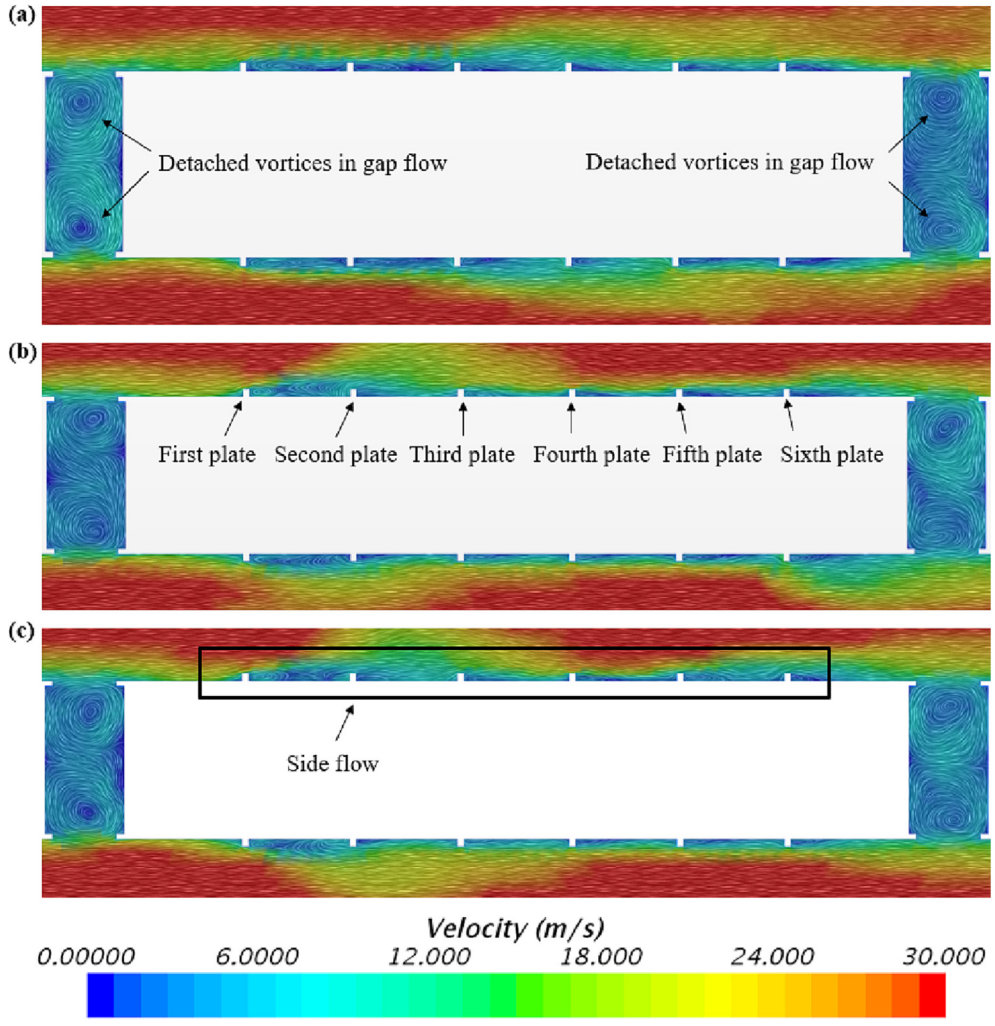

Fig. 10 Flow streamlines in $z = 0.77W$ plane: (a) periodic-boundary condition, (b) full-scale condition, and (c) nine-boxcar condition.

numerical simulations were the same. However, the detached vortex of the side flow under the nine-boxcar condition was stronger than that under the full-scale condition. As shown in Fig. 10(b) and 10(c), the low-speed flow around the side surface of the test wagon under the nine-boxcar condition was much greater than that under the full-scale condition. This was reflected by the mean velocity magnitude curve, which showed that the velocity difference under the nine-boxcar condition was higher than that under the full-scale condition.

The structures of the side flows under the full-scale and nine-boxcar conditions were symmetric about the $y = 0$ plane. Along the flow from left to right, the plates are sequentially arranged from first to sixth across the side surface of the boxcar. As shown in Fig. 10(b) and 10(c), when the flow passed the first plate, a positive pressure zone was generated upstream of the first plate, and a negative pressure zone was generated downstream of the first plate. Meanwhile, a detached vortex was generated downstream of the first plate. As the flow passed the second plate, the velocity of the side flow upstream gradually increased, and the detached vortex generated by the second plate was smaller than that generated by the first plate. A small negative pressure zone was generated downstream of the second plate as well. As the flow passed the third and fourth plates, the velocities of the side flows of the third and fourth plates upstream were higher than that of the second plate, and the detached vortex generated by the third plate was smaller than those of the other plates. As the flow passed the fifth and sixth plates, the velocity of the side flow upstream gradually increased as well, and the detached vortices generated by the fifth and sixth plates were larger than those of the other plates, except for that of the first plate. The negative pressure zones of the plates downstream, from second plate to the sixth plate, gradually increased.

The flow streamlines in the $z = 0.77\ W$ plane for the periodic-boundary and full-scale conditions were compared. There were no significant differences in the vortices of the gap flow upstream and downstream, although the result of the mean pressure under the periodic-boundary condition was lower than that under the full-scale condition. As shown in Fig. 6(c), when the flow passed from the first plate to the sixth plate, the pressure variations upstream and downstream under the periodic-boundary condition were the same as those under the full-scale condition. The side flows under the periodic-boundary and full-scale conditions had little differences. As shown in Fig. 10(a), 10(b), and 10(c), the flow streamlines in the $z = 0.77\ W$ plane were similar for the three

conditions. Thus, the detached vortices and flow field in the $z = 0.77\ W$ plane in three simulations were nearly the same.

3.2.2.1. Pressure field of side surface. The mean pressures of the boxcar side surface under the periodic-boundary, full-scale, and nine-boxcar conditions are shown in Fig. 11(a), 11(b), and Fig. 11(c), respectively. The comparison of the full-scale and nine-boxcar conditions showed that there were no significant differences of their positive pressure zones of the first plate, but the negative pressure zone of first plate under the full-scale condition was larger than that under the nine-boxcar condition. As shown in Fig. 7(c), the reason for this phenomenon was that the mean velocity magnitude at the initial point under the full-scale condition was larger than that under the nine-boxcar condition. As the flow passed the second plate, the positive and negative pressure zones of the second plate in the two numerical simulations reached minimum values. When the flow passed the third plate, the positive and negative pressure zones of the third plate in the two numerical simulations were larger than those of the second plate. When flow passed the fourth, fifth, and sixth plates, the size of the negative pressure zone downstream of the plates gradually increased, and the sizes of the detached vortices generated by plates gradually increased as well.

As shown in Fig. 6(c), the mean pressure curve under the periodic-boundary condition was lower than those of the other numerical simulations. Consequently, only the variation of the pressure field was analyzed in this study. The comparison of the periodic-boundary and full-scale conditions showed that there were no significant differences of the pressure fields at the first plate. As the flow passed the second to sixth plates, the size of the negative pressure zone of second to sixth plates gradually increased in the two numerical simulations, and the maximum of the positive pressure zone of the second to sixth plates in two numerical simulations appeared at the fifth plate. As a result, the mean velocity magnitude and pressure curves between the second and sixth plates reached a maximum at the fifth plate. The comparison of Fig. 11(a), 11(b), and 11 (c) showed that they were nearly the same.

3.2.3. Flow structure of $z = 0.19\ W$ plane

The flow streamlines and Q-Criterion in the $z = 0.19\ W$ plane for the periodic-boundary, full-scale, and nine-boxcar conditions are shown in Fig. 12(a), 12(b), and Fig. 12(c), respectively. Besides, the Q-Criterion in the $z = 0.19\ W$ plane for the whole train in full-scale condition is shown in Fig. 12(d). Q-Criterion usually was used to identify the predominant vortices in computational fluid dynamics. When viscosity is dominant in simulated region, Q-criterion will equal to negative value, and these low-speed detached vortices will not lead a significant effect on aerodynamic performance of test wagon.

Comparing detached vortices in the $z = 0.19\ W$ plane of test wagon, the predominant detached vortices generated by first bogie of periodic-boundary, full-scale, and nine-boxcar simulation are basically similar with each other. Besides, these detached vortices generated by first bogie, not only location, but turbulent energy also are the same in three numerical simulations. Moreover, the migration of predominant detached vortices of periodic-boundary are the same with full-scale and nine-boxcar simulations. As shown in Fig. 12(a), V_{a1} will migrate to upward direction, V_{a2} and V_{a3} will migrate to downward direction. In Fig. 12(b) and 12(c), V_{b1}, V_{b2}, V_{b3}, V_{c1}, V_{c2} and V_{c3} have the same motion as V_{a1}, V_{a2} and V_{a3}, respectively. Thus, the flow structure of $z = 0.19\ W$ plane in

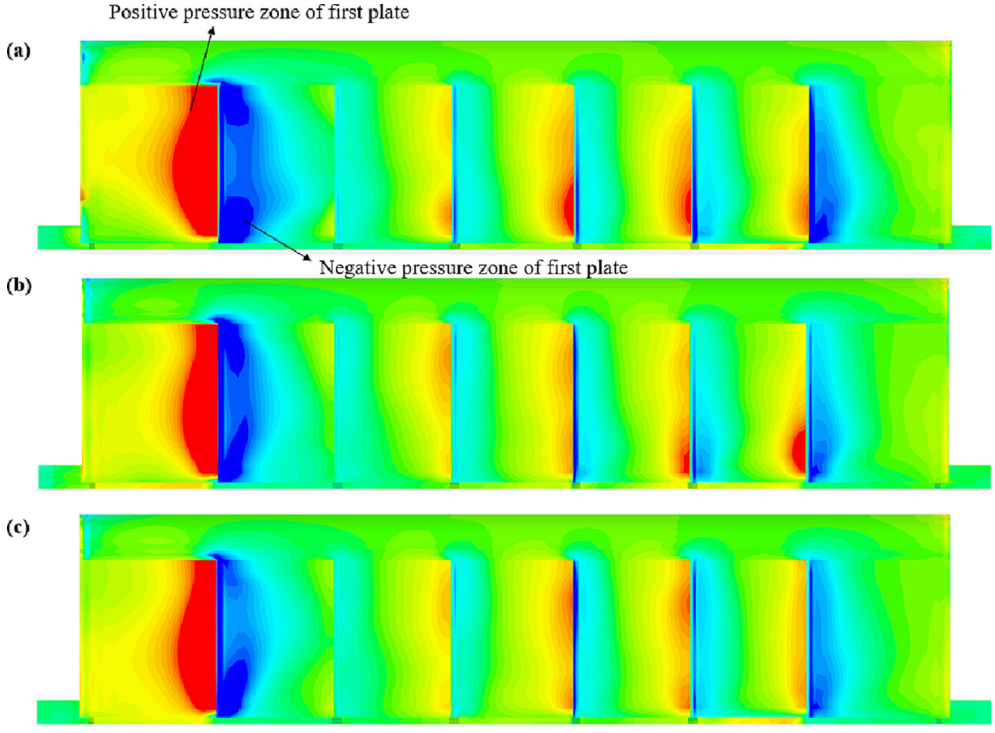

Fig. 11 Pressure fields of test wagon side surface: (a) periodic-boundary condition, (b) full-scale condition, and (c) nine-boxcar condition.

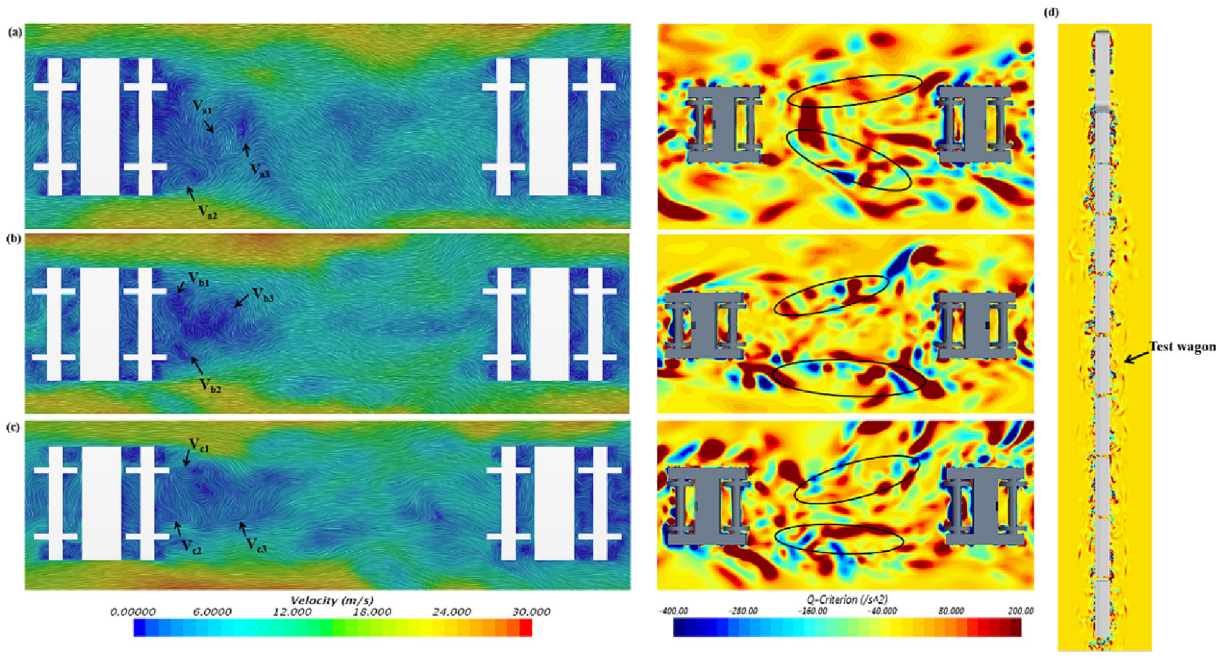

Fig. 12 Flow streamlines and Q-Criterion in $z = 0.19\ W$ plane: (a) periodic-boundary condition, (b) full-scale condition, (c) nine-boxcar condition, and (d) full-scale condition for whole train.

periodic-boundary, full-scale and nine-boxcar simulations is nearly the same.

In a word, the detached flow caused by locomotive has not a significant effect on the test wagon. Besides, the flow structure of $y = 0$, $z = 0.77\ W$ and $z = 0.19\ W$ in periodic-boundary, full-scale and nine-boxcar conditions are basically similar with each other. Moreover, the nine-boxcar condition was used to validate the influence of the locomotive, and it was successful.

4. Conclusion

The purpose of this study was to validate the feasibility of periodic boundaries in freight train aerodynamic simulations. Viscous and pressure drag were separated, and the improved delayed detached eddy simulation approach based on the SST k-ω turbulence model was successfully employed in full-scale, nine-boxcar, and periodic-boundary simulations. Besides, the aerodynamic performances under the nine-boxcar and periodic-boundary simulations were compared with those of the full-scale simulation. The aerodynamic coefficients of the test wagon were investigated, as were the flow field characteristics. Furthermore, the pressure and velocity fields around the test wagon were also analyzed. Finally, following conclusions were drawn:

(1) The pressure drag was the dominant resistance in the 120 km/h freight train simulations, and viscous drag accounted for only 4.7 % of the total resistance.
(2) Periodic boundaries can be used to simulate single-wagon aerodynamic performances in long freight trains under open track conditions. The deviation between the drag coefficients of periodic-boundary and full-scale simulations was 7.6 %. Besides, the agreement between the lift coefficients in the periodic-boundary and full-scale simulations was acceptable. Pressure and velocity fields also could be simulated by the periodic-boundary method, but value of mean pressure deviated from that of the full-scale case, and this deviation caused by software conformal mapping errors. If the pressure and velocity variation is of interest, the periodic-boundary simulation is a good choice. Moreover, the flow structure also has no significant differences in periodic-boundary and full-scale simulations. Thus, characteristics of flow field could still be simulated using periodic-boundary method.
(3) The locomotive has not a significant influence on the aerodynamic performance of the fifth wagon in full-scale simulation, and the deviation between the drag coefficients in the full-scale and nine-boxcar simulations are 5.7 %. Besides, the lift coefficients of test wagon in the full-scale and nine-boxcar simulations are acceptable. The pressure, velocity, and flow fields of test wagon in the full-scale and nine-boxcar simulations were nearly the same.

Declaration of Competing Interest

The authors declare that they have no known competing financial interests or personal relationships that could have appeared to influence the work reported in this paper.

Acknowledgments

The authors acknowledge the computational resources provided by the High-Speed Train Research Centre of Central South University, China. This work was supported by the Science and Technology Innovation Program of Hunan Pro-

vince (Grant No. 2022RC3040), the Fundamental Research Funds for the Central University of Central South University (No. 1053320210633), and the Fundamental Research Funds for the Central University of Central South University (No. 1053320211135).

References

[1] Z. Guo, T. Liu, Y. Xia, Z. Liu, Aerodynamic influence of the clearance under the cowcatcher of a high-speed train, J. Wind Eng. Ind. Aerodyn. 220 (2022), https://doi.org/10.1016/j.jweia.2021.104844.

[2] V.A. Golovanevskiy, V.V. Chmovzh, Y.V. Girka, On the optimal model configuration for aerodynamic modeling of open cargo railway train, J. Wind Eng. Ind. Aerodyn. 107–108 (1) (2012) 131–139.

[3] C. Chen, W. Li, Y. Liu, X. Wei, Exploration of key traction-running equipment and its problems on heavy-haul trains and research on technology development, Trans. Safety and Environ. 2 (3) (2020) 161–182, https://doi.org/10.1093/tse/tdaa019.

[4] S. Maleki, D. Burton, M.C. Thompson, Flow structure between freight train containers with implications for aerodynamic drag, J. Wind Eng. Ind. Aerodyn. 188 (4) (2019) 194–206, https://doi.org/10.1016/j.jweia.2019.02.007.

[5] C. Li, D. Burton, M. Kost, J. Sheridan, M.C. Thompson, Flow topology of a container train wagon subjected to varying local loading configurations, J. Wind Eng. Ind. Aerodyn. 169 (4) (2017) 12–29, https://doi.org/10.1016/j.jweia.2017.06.011.

[6] S. Maleki, D. Burton, M.C. Thompson, On the flow past and forces on double-stacked wagons within a freight train under cross-wind, J. Wind Eng. Ind. Aerodyn. 206 (4) (2020), https://doi.org/10.1016/j.jweia.2020.104224 104224.

[7] J. Östh, S. Krajnović, A study of the aerodynamics of a generic container freight wagon using Large-Eddy Simulation, J. Fluids Struct. 44 (5) (2014) 31–51, https://doi.org/10.1016/j.jfluidstructs.2013.09.017.

[8] J.R. Bell, D. Burton, M.C. Thompson, A.H. Herbst, J. Sheridan, Dynamics of trailing vortices in the wake of a generic high-speed train, J. Fluids Struct. 65 (2016) 238–256, https://doi.org/10.1016/j.jfluidstructs.2016.06.003.

[9] X. Huo, T. Liu, Z. Chen, W. Li, J. Niu, H. Gao, Aerodynamic characteristic of double-connected train groups composed of different kinds of high-speed trains under crosswinds: a comparison study, Alex. Eng. J. 1 (1) (2022) 1, https://doi.org/10.1016/j.aej.2022.09.011.

[10] D. Soper, C. Baker, M. Sterling, Experimental investigation of the slipstream development around a container freight train using a moving model facility, J. Wind Eng. Ind. Aerodyn. 135 (3) (2014) 105–117, https://doi.org/10.1016/j.jweia.2014.10.001.

[11] S. Watkins, J.W. Saunders, H. Kumar, Aerodynamic drag reduction of goods trains Retrieved fro'm, J. Wind Eng. Ind. Aerodyn. 40 (2) (1992) 147–178. https://www.sciencedirect.com/science/article/pii/016761059290363F, https://doi.org/10.1016/0167-6105(92)90363-f.

[12] H. Sadat-Hosseini, P. Carrica, F. Stern, N. Umeda, H. Hashimoto, S. Yamamura, A. Mastuda, CFD, system-based and EFD study of ship dynamic instability events: surf-riding, periodic motion, and broaching, Ocean Eng. 38 (1) (2011) 88–110, https://doi.org/10.1016/j.oceaneng.2010.09.016.

[13] M. Jbeili, J. Zhang, The generalized periodic boundary condition for microscopic simulations of heat transfer in heterogeneous materials, Int. J. Heat Mass Transf. 173 (4) (2021), https://doi.org/10.1016/j.ijheatmasstransfer.2021.121200 121200.

[14] L. Qian, J. Deng, Z. Li, W. Chen, H. Yu, Y. Sun, Theoretical research on two-phase flow instability in parallel channels under periodic heaving motion condition, Ann. Nucl. Energy 157 (2021), https://doi.org/10.1016/j.anucene.2021.108263 108263.

[15] Z. Huang, N. Chang, Aerodynamic forces acting on a box car running on the railway alone with the wind-break wall under strong cross-wind, J. Railway Sci. Eng. 9 (04) (2012) 101–105, https://doi.org/10.19713/j.cnki.43-1423/u.2012.04.019.

[16] Y. Xia, T. Liu, H. Gu, Z. Guo, Z. Chen, W. Li, L. Li, Aerodynamic effects of the gap spacing between adjacent vehicles on wind tunnel train models, Eng. Applications of Comput. Fluid Mech. 14 (1) (2020) 835–852.

[17] Y. Xia, T. Liu, W. Li, X. Dong, Z. Chen, Z. Guo, Numerical comparisons of the aerodynamic performances of wind-tunnel train models with different inter-carriage gap spacings under crosswind, J. Wind Eng. Ind. Aerodyn. 214 (7–8) (2021), https://doi.org/10.1016/j.jweia.2021.104680 104680.

[18] X. Dong, T. Liu, Z. Shi, Y. Xia, F. Yang, Z. Chen, Influence of porosity of reformed earth embankment windbreak wall on flow field and displacement of catenary under crosswinds, J. Wind Eng. Ind. Aerodyn. 214 (10–11) (2021), https://doi.org/10.1016/j.jweia.2021.104652 104652.

[19] Z. Guo, T. Liu, H. Hemida, Z. Chen, H. Liu, Numerical simulation of the aerodynamic characteristics of double unit train, Eng. Applications of Comput. Fluid Mech. 14 (1) (2020) 910–922, https://doi.org/10.1080/19942060.2020.1784798.

[20] J. Zhang, J. Wang, X. Tan, G. Gao, X. Xiong, Detached eddy simulation of flow characteristics around railway embankments and the layout of anemometers, J. Wind Eng. Ind. Aerodyn. 193 (F3) (2019), https://doi.org/10.1016/j.jweia.2019.103968 103968.

[21] Z.-K. Sun, T.-T. Wang, F. Wu, Numerical investigation of influence of pantograph parameters and train length on aerodynamic drag of high-speed train, J. Cent. South Univ. 27 (4) (2020) 1334–1350, https://doi.org/10.1007/s11771-020-4370-6.

[22] Z. Chen, T. Liu, M. Yu, G. Chen, M. Chen, Z. Guo, Experimental and numerical research on wind characteristics affected by actual mountain ridges and windbreaks: a case study of the Lanzhou-Xinjiang high-speed railway, Eng. Applications of Comput. Fluid Mech. 14 (1) (2020) 1385–1403, https://doi.org/10.1080/19942060.2020.1831963.

[23] J. Van Doormaal, G. Raithby, Enhancements of the SIMPLE method for predicting incompressible fluid flows, Numerical Heat Transfer 7 (2) (1984) 147–163, https://doi.org/10.1080/01495728408961817.

[24] T. Liu, Z. Chen, X. Zhou, J. Zhang, A CFD analysis of the aerodynamics of a high-speed train passing through a windbreak transition under crosswind, Eng. Applications of Comput. Fluid Mech. 12 (1) (2017) 137–151.

[25] BS EN 14067-6-2018 Requirements and test procedures for cross wind assessment.

[26] J.-Q. Niu, X.-F. Liang, D. Zhou, Y.-M. Wang, Numerical investigation of the aerodynamic characteristics of a train subjected to different ground conditions in proceedings of the institution of mechanical engineers, part F, J. Rail and Rapid Transit 232 (10) (2018) 2371–2384, https://doi.org/10.1177/0954409718770345.

[27] S. Krajnović, L. Davidson, Influence of floor motions in wind tunnels on the aerodynamics of road vehicles, J. Wind Eng. Ind. Aerodyn. 93 (9) (2005) 677–696, https://doi.org/10.1016/j.jweia.2005.05.002.

[28] R.K. Strachan, K. Knowles, N.J. Lawson, The vortex structure behind an Ahmed reference model in the presence of a moving ground plane, Exp. Fluids 42 (5) (2007) 659–669, https://doi.org/10.1007/s00348-007-0270-x.

[29] Siemens, STAR-CCM+ User Guide, Release 12 (2017) 02.